B-type Fabric in the Mantle Wedge: Insights from High-resolution Non-Newtonian Subduction Zone Models

Erik A. Kneller
University of Michigan,
2005

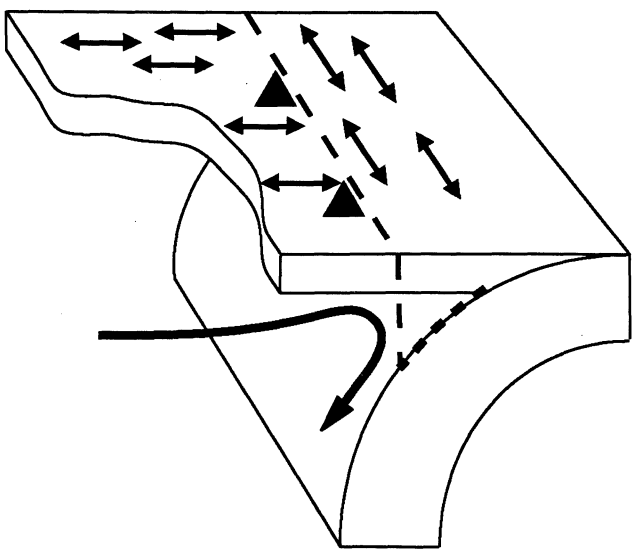


THE UNIVERSITY OF MICHIGAN
LIBRARIES
THE UNIVERSITY OF MICHIGAN
1817

Erik Arthur Kneller

B-type Fabric in the Mantle Wedge: Insights from High-resolution Non-Newtonian Subduction Zone Models

submitted in partial fulfillment
of the requirements for the degree of
Master of Science in Geology
Department of Geological Sciences
The University of Michigan

Accepted by:

Peter van Keken Signature	PETER VAN KEKEN Name	4/18/05 Date
Larry Ruff Signature	Larry Ruff Name	Apr 11 2005 Date
Joel D Blum Department Chair	Joel D Blum Name	4/19/05 Date

I hereby grant the University of Michigan, its heirs and assigns, the non-exclusive right to reproduce and distribute single copies of my thesis, in whole or in part, in any format. I represent and warrant to the University of Michigan that the thesis is an original work, does not infringe or violate any rights of others, and that I make these grants as the sole owner of the rights to my thesis. I understand that I will not receive royalties for any reproduction of this thesis.

☑ Permission granted.

☐ Permission granted to copy after: _____
Date

☐ Permission declined.

Erik Kneller
Author Signature

Abstract

Several hypotheses have been proposed to explain trench-parallel shear wave splitting in the mantle wedge of subduction zones. These include 3-D flow effects, parallel melt filled cracks, and B-type olivine fabric. We predict the distribution of B-type and other fabrics with high-resolution thermal and stress models of subduction zones. A composite viscous rheology is used that incorporates wet diffusion creep, wet dislocation creep, and a stress-limiting approximated Peierls creep law. Rheological parameters for dislocation and diffusion creep are based on deformation experiments. The effects of variable viscous coupling between the slab and mantle are explored using kinematic boundary conditions that change along the top of the slab. Two end-member models are observed, which depend on the depth of partial viscous coupling between the slab and mantle: (1) deep partial coupling which gives rise to cold, high-stress conditions in the fore-arc mantle and high-temperature, low-stress conditions in the arc and back-arc mantle (2) full viscous coupling at the base of a 40 km conducting lid which is characterized by high temperature and low stress. The case with deep partial coupling, which produces a better match with attenuation tomography and heat flow, shows a large region with suitable conditions for B-type fabric in the fore-arc mantle, and a rapid transition toward the back arc to conditions that are more suitable for A, C, or E type fabrics. Full viscous coupling gives rise to high-temperature, low-stress conditions unsuitable for B-type fabric. Our modeling predicts that the best candidates for regions with B-type fabric are the fore-arc mantle and a cold 10-15 km layer above the slab.

Introduction

Deformation in the mantle wedge of subduction zones causes lattice preferred orientation (LPO) which in turn affects the directional dependence of seismic wave velocity. This provides the potential to map deformation fabric with seismological observations and thus gain insight into the pattern of solid-state flow. The pattern of anisotropy in subduction zones is diverse and poorly understood but advances in mineral physics and new seismic observations provide improved constraints. Deformation experiments have yielded new insights into the diversity of olivine fabric [1, 2] and new studies of anisotropy are increasing our knowledge of deformation fabric in the mantle wedge [3, 4]. Progress is also being made with seismology toward better constraining the geometry of the slab and subducting crust and the distribution of temperature, water, and partial melt [5, 6]. These advances can be coupled with geodynamics to form physically more realistic models of subduction zone processes. This work uses recent deformation experiments and geodynamic models of the mantle wedge to investigate the possibility that water-induced fabric transitions play an important role in controlling the pattern of seismic anisotropy in the mantle wedge.

Seismic anisotropy can be caused by parallel alignment of isotropic layers and cracks in the mantle and crust, and LPO [7, 8]. Studies of the distribution of anisotropy in subduction zones suggest that LPO is the dominant cause of seismic anisotropy [7, 9, 10]. A variety of fabrics have been observed in naturally deformed olivine aggregates from a range of tectonic settings [11–16]. The most common olivine fabric is A-type, which has a fast-axis orientation subparallel to the shear direction [12]. This fabric has been used to explain convergence-parallel fast directions from surface-wave and P_n tomography in mid-ocean ridge systems [8, 17]. However, this simple model fails for subduction zones where the fast direction varies with respect to convergence direction and often shows trench-parallel fast directions [5, 10, 18–20]. In some cases trench-parallel fast directions may be caused by anisotropy within or beneath the slab. For example, in the Kamchatka fore arc, teleseismic SKS splitting is trench-parallel [21], but both receiver functions [22] and shear-wave splitting from events in the slab [23] indicate a trench-normal fast axis with weak splitting. This suggests a trench-normal fast axis in the fore arc mantle wedge and a trench-parallel fast axis beneath the slab.

Several hypotheses have been proposed that use LPO to explain trench-parallel shear wave splitting in subduction zones. These hypotheses include LPO controlled by 3-D flow effects [24], water-induced fabric transitions [1, 25], and strain partitioning via melt networks [26]. The evidence for abundant water in subduction zones [25] suggests that water-induced fabric transitions in olivine is a mechanism common to

all subduction environments. However, the diversity of patterns of anisotropy in subduction zones makes it difficult to ascribe a single mechanism and it is possible that a variety of mechanisms are at play.

Recent deformation experiments have explored the influence of variety of physico-chemical conditions on olivine fabrics [1, 2]. Combined with a theory [27] and observations on naturally deformed peridotites [13, 14, 16, 28, 29] we now have a better idea about the variation of olivine LPO with water content, stress, and temperature. The A-type fabric, assumed in the previous interpretation of seismic anisotropy, is a dominant fabric under low stress and low water content, whereas at higher water contents, other types of olivine fabrics become important (B-, C- and E-types) (Figure 1). Particularly important is the B-type fabric with which olivine [001] axis is subparallel to the flow direction and olivine (010) plane is subparallel to the flow plane. For this type of LPO, olivine [100] axis is normal to the flow direction and consequently the direction of polarization of the faster S-wave is normal to the flow direction. Other fabrics (A-, C- and E-type fabrics) result in similar shear wave splitting: the direction of polarization of the faster S-wave is subparallel to the flow direction. The recent studies mentioned above show that the B-type fabric is dominant over C-type (or E- or A-type) fabric at relatively high stress and high temperatures. The boundary between B- and C-fabrics is linear in temperature and stress [27, 29]. This linear boundary can be extrapolated from experimental conditions to give a B-C transition temperature of 750-950 °C at 10 MPa (Figure 2). We estimate the distribution of B-type and other fabrics by predicting the distribution of temperature, stress, and strain rate with numerical models. Regions with stress greater than 5 MPa, temperature less than 900 °C, and strain rate on the order of $10^{-14}\mathrm{s}^{-1}$ are considered good candidates for B-type fabric.

Modeling Approach

The models presented in this paper implement a kinematic-dynamic method where the slab and overriding lid are kinematicaly described and mantle wedge flow is dynamically modeled (Figure 3). Flow in the mantle wedge is driven by a kinematic boundary condition at the top of the slab. This is similar to the models described by [30–34]. We particularly follow the approach of [35].

The details of the wedge geometry are uncertain, in particular in regard to the position of the rigid overriding plate and the position of the corner point in the wedge return flow. Most previous models have assumed that the corner point is the down-dip limit of the seismogenic zone, but it is likely that non-seismic slip and shear localization extend to further depth. Since we only model viscous deformation in the mantle

wedge at very long geological time scales we cannot account self-consistently for the non-seismic slip down-dip from the seismogenic zone. Furthermore, shear localization in the slab-wedge interface, which could be due to the presence of weak minerals such as talc and serpentine [36–38], is not accounted for with our olivine rheology. As discussed below, we make a simple approximation that non-viscous deformation and shear localization can be accounted for by reducing the coupling of the slab to the overlying wedge at shallow depths and allow a transition to full coupling at larger depths.

The finite element package SEPRAN is used for mesh generation and the numerical approximation of solutions for governing equations (http://ta.twi.tudelft.nl/sepran/sepran.html). The systems of equations generated by the finite element method are solved using a conjugate gradient iteration (Bi-CGSTAB) [39].

Flow in the mantle wedge is governed by the conservation of momentum for an incompressible infinite Prandtl number fluid without buoyancy forces:

$$-\nabla P + \nabla(\eta \cdot \dot{\boldsymbol{\epsilon}}) = 0 \tag{1}$$

where $\dot{\boldsymbol{\epsilon}}$ is the strain rate tensor, η is effective viscosity, and P is dynamic pressure. The conservation of mass for an incompressible fluid is expressed as

$$\nabla \cdot \mathbf{u} = 0 \tag{2}$$

where $\mathbf{u}$ is velocity. Eq. (1) and (2) are solved for pressure and velocity on a mesh composed of linear Taylor-Hood triangles [40].

A stress-free inflow/outflow boundary condition for eq. (1) is present along the right hand boundary below 40 km. Velocity boundary conditions for eq. (1) are prescribed along the top of the slab and at the base of the conducting lid. The velocity boundary condition is reduced along the top of the slab from the bottom of the conducting lid to around 70 km (Figure 3b). The magnitude of the boundary condition is increased in a linear manner to slab velocity over 10 km. This is a simple way to parameterize the effects of non-seismic slip and shear localization. There are three main modes of long time scale viscous coupling in our models: (1) full viscous decoupling in the seismogenic zone, which simulates brittle stick-slip deformation over long periods of time, (2) partial coupling in the fore arc mantle, which simulates shear localization and non-seismic slip, and (3) full viscous coupling below a depth of 70 km. Viscous coupling as defined in this paper should not be confused with short time scale seismic coupling.

The conservation of energy for steady-state conditions and negligible viscous dissipation takes the form of the convection-diffusion equation with heat production:

$$\rho c_p (\mathbf{u} \cdot \nabla) T = \nabla \cdot (k \nabla T) + Q + Q_{sh} \tag{3}$$

where k is thermal conductivity, T is temperature, Q is radioactive heat production, Q_{sh} is shear heating, c_p is specific heat, and ρ is density. Specific heat is 1250 J/kg/K and density is 3300 kg/m^3. Shear heating is defined with a delta function:

$$Q_{sh} = Q\delta(x_{interface}) \tag{4}$$

where Q is the magnitude of shear heating, and $x_{interface}$ is the position of the seismogenic zone. The seismogenic zone extends from the trench to the base of the conducting lid at 40 km and Q is 29 mW/m^2. Heat production is 1.3 μW/m^3 from 0-15 km (upper crust) and 0.27 μW/m^3 from 15-30 km (lower crust). Streamline upwinding is used for the solution of eq. (3) due to the strong advective term.

Fixed-temperature boundary conditions for the convection-diffusion equation are present along the top of the model (T=0), along the left inflow boundary (half-space cooling model), and along the right inflow boundary. The fixed temperature boundary condition along the upper 95 km of the right inflow boundary is described by a continental geotherm with crustal heat production as described above and surface heat flow equal to 65 mW/m^2. A mantle potential temperature of 1450 °C is prescribed below 95 km to the depth of the outflow boundary condition.

Eq. (1-3) are solved by the Picard iteration to relative accuracy of 10^{-6}. Resolution varies from 0.25 to 1 km in the fore-arc, back-arc mantle, and above the slab (Figure 4) giving rise to viscosity gradients in elements less than a factor of 3. High resolution is necessary for accurate calculation of $\mathbf{u}$ and T because of large viscosity gradients in thermal boundary layers and the presence of a pressure singularity at the corner point [35]. Slab dip is either 45° or defined by a polynomial fit to seismic data. Polynomial descriptions have smooth variation in curvature and produce more accurate calculation of velocity for non-Newtonian calculations.

Rheology

A general steady-state rheological law for olivine at high temperatures can be expressed as

$$\dot{\epsilon}_{ij} = A\left(\frac{b}{d}\right)^m exp\left[-\frac{(E+PV)}{RT}\right]\sigma^{n-1}\,\sigma_{ij} \tag{5}$$

where where $\dot{\epsilon}_{ij}$ is the ij-th component of the strain rate tensor, σ_{ij} is the ij-th component of the deviatoric stress tensor, σ is the second invariant of the deviatoric stress tensor, b is the Burgers vector, d is grain size, E is activation energy, P is pressure, V is activation volume, R is the gas constant, T is temperature, n is

the stress exponent, m is the grain size exponent, and A is a constant [41]. The strain rate tensor is defined as

$$\dot{\epsilon}_{ij} = \left(\frac{du_i}{dx_j} + \frac{du_j}{dx_i} \right) \tag{6}$$

Second invariants of the stress and strain rate tensors are defined as

$$\sigma = \sqrt{\frac{1}{2} \sum \sigma_{ij} \sigma_{ij}} \tag{7}$$

and

$$\dot{\epsilon} = \sqrt{\frac{1}{2} \sum \dot{\epsilon}_{ij} \dot{\epsilon}_{ij}} \tag{8}$$

respectively. Eq. (7) and (8) are used to define an effective viscosity

$$\eta = \frac{\sigma}{\dot{\epsilon}} \tag{9}$$

For dislocation creep m = 0 and n >1, which gives rise to a power-law rheology

$$\dot{\epsilon}_{ij} = A \, exp\left[-\frac{(E + PV)}{RT} \right] \sigma^{n-1} \sigma_{ij} \tag{10}$$

For computational purposes the effective viscosity for power-law rheology is defined in terms of $\dot{\epsilon}$ via the inversion of equation 10

$$\eta_{disloc} = A^{-\frac{1}{n}} \, exp\left[-\frac{(E + PV)}{RT} \right] \dot{\epsilon}^{\frac{1-n}{n}} \tag{11}$$

Newtonian diffusion creep has n = 1 and m >1 which gives the following expression for effective viscosity

$$\eta_{diff} = A^{-1} \left(\frac{d}{b} \right)^m exp\left[\frac{(E + PV)}{RT} \right] \tag{12}$$

Effective viscosity at low temperature is given by an approximated Peierls rheology

$$\eta_{pei} = \tau_y \dot{\epsilon}_y^{-\frac{1}{n_y}} \dot{\epsilon}^{\frac{1}{n_y} - 1} \tag{13}$$

where τ_y is a yield stress, $\dot{\epsilon}_y$ is a yield strain, and n_y is a constant [42] (Table 1). All three creep mechanisms occur in parallel which leads to the following effective composite viscosity

$$\eta = \left(\frac{1}{\eta_{disloc}} + \frac{1}{\eta_{diff}} + \frac{1}{\eta_{pei}} \right)^{-1} \tag{14}$$

The dislocation creep law is expressed in terms of parallel dry and wet mechanisms

$$\dot{\epsilon} = \dot{\epsilon}_{disloc,dry} + \dot{\epsilon}_{disloc,wet} \tag{15}$$

where

$$\dot{\epsilon}_{disloc,dry} = A_{disloc,dry}\, exp\left[-\frac{(E_{disloc,dry} + PV_{disloc,dry})}{RT}\right]\sigma^n \tag{16}$$

and

$$\dot{\epsilon}_{disloc,wet} = A_{disloc,wet}\, C_{OH}^r\, exp\left[-\frac{(E_{disloc,wet} + PV_{disloc,wet})}{RT}\right]\sigma^n \tag{17}$$

The concentration water in ppm H/Si is denoted by C_{OH}. Parameters for the dislocation creep law are for a closed system [43] (Table 1). The creep laws for dry and saturated diffusion creep [44] (Table 1) are combined into a law for conditions with variable water content [45]

$$\dot{\epsilon} = \dot{\epsilon}_{diff,dry} + (\dot{\epsilon}_{diff,sat} - \dot{\epsilon}_{diff,dry})\left(\frac{C_{OH}}{C_{OH}^{max}}\right)^q \tag{18}$$

where

$$\dot{\epsilon}_{diff,dry} = A_{diff,dry}\left(\frac{b}{d}\right)^m exp\left[-\frac{(E_{diff,dry} + PV_{diff,dry})}{RT}\right]\sigma \tag{19}$$

and

$$\dot{\epsilon}_{diff,sat} = A_{diff,sat}\left(\frac{b}{d}\right)^m exp\left[-\frac{(E_{diff,sat} + PV_{diff,sat})}{RT}\right]\sigma \tag{20}$$

Dislocation creep dominates deformation for grain sizes around 1 mm and typical mantle wedge temperature and strain rate except in very cold low strain rate boundary layers. Grain sizes around 0.1 mm lead to fairly large regions dominated by diffusion creep where strain rate is moderate.

Results

We test several cases with a simple slab geometry: (1) dry composite rheology with full viscous coupling starting at a depth of 40 km, (2) case 1 with 1000 ppm H/Si, and (3) wet composite rheology with partial coupling down to 70 km. Model parameters for each case can be found in table 2.

Case 1 gives rise to very high temperatures in the fore-arc mantle wedge (Figure 5). This is similar to the results of [35, 46]. Temperature ranges from 1000-1250 °C which would facilitate melting in the mantle 50-60 km from the trench [33]. High temperatures and non-Newtonian rheology produce a relatively low-stress environment (< 3 MPa) throughout the entire mantle wedge. Temperature dependence of viscosity gives rise to the entrainment of cold mantle-wedge material in the slab-wedge interface and the focusing of

cornerflow into the corner point. Two low viscosity lobes develop in the core of the wedge where strain rate is high.

A water content of 1000 ppm H/Si [47] is added to the mantle wedge in figure 6. This leads to a uniform viscosity reduction of around an order of magnitude, an increase in strain rate, and a stress reduction of around an order of magnitude. Stress is now less than 1 MPa for most of the mantle wedge. Increasing the water content to 3000 ppm and localizing the distribution of water to a 30 km layer above the slab does not modify the pattern of flow significantly. This is a consequence of the temperature dependence of viscosity which causes cold boundary layers to remain rigid after the order of magnitude viscosity reduction induced by water. The low stress and high temperature observed for case 2 would hinder the development of B-type fabric.

The thermal structure of the fore-arc environment is modified considerably if the slab and mantle are only partially coupled [48]. Partial viscous coupling limits the ability of the slab to entrain mantle in the slab-wedge interface thus decreasing the extent to which hot material can be focused into the fore-arc mantle. Figure 7 is an example of wet composite rheology with partial coupling between the slab and mantle down to 70 km. The depth at which the slab and mantle become fully coupled controls the height of penetration of the hot tongue of cornerflow, which is constrained to first order by the position of the volcanic front. A large temperature gradient from the wedge core to fore-arc mantle (30-40°C/km) causes a rapid transition from conditions suitable for C-type fabric in the hot core of the mantle wedge to those more suitable for B-type in the fore arc. This C-B transition occurs over 10-15 km. Colder temperatures in the fore-arc mantle wedge give rise to larger stress (50-70 MPa). However, more realistic low-temperature rheological models are necessary to model deviatoric stress accurately in the colder regions of the mantle wedge. If we reduce the speed of subduction to around 5 cm/yr, a cold high-stress boundary layer develops in the slab-wedge interface. Therefore conditions in this layer are also suitable for B-type fabric if subduction is sluggish.

Cases 4 and 5 use the geometry of the Honshu subduction system [35] (Figure 8, Table 2). The case with full coupling starting at the base of the 40 km conducting lid gives rise to a very shallow 1200°C tongue of mantle 80 km trenchward of the volcanic arc. Case 5 has partial viscous coupling and the low-temperature, high-stress nose observed in case 3. A comparison of surface heat flow for cases 4 and 5 shows that deep partial coupling gives rise to a better match with observations (Figure 8c). The deep partial coupling case also is more consistent with attenuation and velocity tomography both of which show a relatively cold fore-arc mantle [3, 49–51]. Furthermore, the deep transition from partial to full coupling and olivine rheology produces a localized region with large temperature gradients (80 °C/km) along the slab-wedge interface

which corresponds to a maximum in intermediate depth seismic activity beneath Honshu [50].

Discussion

The thermal models presented in this work show that the thermal structure of the fore-arc mantle depends strongly on the depth of full viscous coupling between the slab and mantle. This coupling transition is constrained by the position of the volcanic front below which hot mantle must be transported by wedge flow [33]. The height of the transition is constrained by heat flow data [31], which unfortunately is sparse for most arcs, and the lack of fore-arc magmatism. Cases with partial viscous coupling down to 70 km better match attenuation and heat flow. Partial viscous coupling in the slab-mantle interface may be caused by the presence of low-temperature phyllosilicates such as talc and serpentine [36–38]. Both serpentine and talc are weak minerals and could cause shear localization in the slab-wedge interface. The abundance of low density serpentine may also facilitate viscous decoupling in the fore arc. In this scenario a serpentinized fore-arc mantle is isolated from large scale convective flow due to its positive buoyancy. Slow coseismic slip below the seismogenic zone associated with large subduction zone earthquakes [52, 53] could also give rise to decreased viscous decoupling between the slab and mantle. As discussed above, we simulate the effect of partial coupling by modifying the kinematic boundary condition at the top of the slab. Further work in mineral physics and geodynamic modeling is needed to better understand the physical properties and behavior of materials in the cold fore-arc mantle.

Models with deep partial coupling predict suitable thermal and stress conditions for B-type fabric in the fore-arc mantle. The core of the wedge is dominated by high-temperature, low-stress conditions that are more suitable for C-type, E-type or A-type fabric depending on water content. A cold, 10-15 km thick, high-stress thermal boundary layer above the slab is also a candidate for B-type fabric if subduction rate is less than 5 cm/yr.

For the partially coupled case, the position of the volcanic front is predicted to mark the transition from A, C, or E-type to B-type fabric (Figure 9). Two end-member patterns of subduction zone anisotropy are expected from our predictions of the distribution of B-type fabric. If deformation is dominated by 2-D coupling between the slab and mantle, the fast direction in the fore-arc mantle would be trench-parallel while trench-perpendicular fast directions would be observed in the arc and back arc (Figure 9a). A significant component of trench-parallel flow would produce the opposite pattern assuming that slab-wedge coupling

still dominates the overall pattern of flow (Figure 9b).

Shear wave splitting results from Northern Honshu [3, 54] and the Central Andes [4, 19] show the general pattern of Figure 9a where 2-D cornerflow gives rise to trench-normal flow. Anisotropy in Northern Honshu shows an abrupt transition from trench-parallel fast directions in the fore arc to trench-perpendicular in the arc and back arc [3]. A similar abrupt transition is observed in S wave tomography where fast velocity in the fore arc rapidly changes to slow velocity in the arc and back-arc mantle [3, 50]. Honshu thermal models consistent with these seismic observation have partial viscous coupling down to 70 km and predict that B-type fabric is stable in the fore-arc environment (Figure 8b). This picture is consistent with the B-type fabric model for mantle wedge anisotropy that requires a cold fore-arc mantle and hot arc and back-arc mantle. Anisotropy in the Central Andes shows similar pattern to Honshu where trench-parallel fast directions occur close to the trench and trench-normal fast directions are observed in the back arc [4, 19]. Our models suggest that the region in the Central Andes with trench-parallel fast directions could be dominated by cold temperatures and high stress. We predict that B-type may play an important role here as well.

Shear wave splitting from sections of the Kamchatka [23] and Central Alaska subduction systems [55] are similar to the pattern shown in Figure 9b. These subduction zones are also candidates for the B-type fabric hypothesis if a significant component of trench-parallel flow is present.

Several subduction systems show trench-parallel shear wave splitting in the arc and back-arc mantle where we predict high-temperature and low-stress conditions that are not suitable for B-type fabric. These systems include Tonga [20], Eastern Aleutians [10], and Central Honshu [18]. Our models predict that a more probable cause for trench-parallel anisotropy in these subduction systems is trench-parallel flow with A or E-type fabric. Trench-parallel anisotropy in the arc mantle could also be caused by parallel melt filled cracks as proposed by [18]

Conclusions

We produce steady-state subduction zone models with deep partial viscous coupling that are consistent with attenuation and velocity tomography and heat flow. These models predict that temperature and stress in fore-arc mantle and slab-wedge interface are suitable for B-type fabric. The core of the mantle wedge is characterized by high temperatures and low stress conditions more suitable for A, C, or E-type fabrics depending on water content. The B-type fabric anisotropy hypothesis adequately predicts the pattern of

anisotropy in Northern Honshu and Central Andes. If a significant component of trench-parallel flow is present and the large scale flow pattern is still dominated by slab-mantle coupling than B-type fabric could also explain anisotropy in parts of the Kamchatka and Alaska subduction systems.

Acknowledgments

This research is supported by the National Science Foundation.

References

[1] H. Jung, S. Karato, Water-induced fabric transition in olivine, Science, 293 (2001) 1460–1463.

[2] I. Katayama, H. Jung, S. Karato, New type of olivine fabric from deformation experiments at modest water content and low stress, Geology, 32 (2004) 1045–1048.

[3] J. Nakajima, A. Hasegawa, Shear-wave polarization anisotropy and subduction-induced flow in the mantle wedge of northeastern Japan, Earth Planet. Sci. Lett., 225 (2004) 365–377.

[4] M. L. Anderson, G. Zandt, E. Triep, M. Fouch, S. Beck, Anisotropy and mantle flow in the chile-argentina subduction zone from shear wave splitting analysis, Geophys. Res. Lett., 31 (2004), doi: 10.1029/2004GL020906.

[5] D. A. Wiens, G. P. Smith, Seismological constraints on the structure and flow patterns within the mantle wedge, in: J. Eiler (ed.), Inside the subduction factory, AGU, Washington, D.C., 2003, Geophysical Monograph 138, pp. 83-105.

[6] P. E. van Keken, The structure and dynamics of the mantle wedge, Earth Planet. Sci. Lett., 215 (2003) 323–338.

[7] M. K. Savage, Seismic anisotropy and mantle deformation: what have we learned from shear wave splitting?, Rev. Geophys., 37 (1999) 65–106.

[8] J. Park, V. Levin, Seismic anisotropy: tracing plate dynamics in the mantle, Science, 296 (2002) 485–489.

[9] M. J. Fouch, K. M. Fischer, Shear wave anisotropy in the Mariana subduction zone, Geophys. Res. Lett., 25 (1998) 1221–1224.

[10] X. Yang, K. M. Fischer, G. Abers, Seismic anisotropy beneath the Shumagin Islands segment of the Aleutian-Alaska subduction zone, J. Geophys. Res., 100 (1995) 18165–18177.

[11] A. L. Littlejohn, H. J. Greenwood, Lherzolite Nodules in Basalts from British Columbia, Canada, Can. J. Earth Sci., 11 (1996) 1288–1308.

[12] B. W. Ismaïl, D. Mainprice, An olivine fabric database: an overview of upper mantle fabrics and seismic anisotropy, Tectonophysics, 196 (1998) 145–157.

[13] K. Frese, V. Trommsdorff, K. Kunze, Olivine [100] normal to foliation: lattice preferred orientation in prograde garnet peridotite formed at high H_2O activity, Cima di Gagnone (Central Alps), Contrib. Mineral. Petrol., 145 (2003) 75–86.

[14] L. Mehl, B. R. Hacker, G. Hirth, P. B. Kelemen, Arc-parallel flow within the mantle wedge evidence from the accreted Talkeetna arc, south central Alaska, J. Geophys. Res., 108 (2003), doi:10.1029/2002JB002233.

[15] T. Sawaguchi, Deformation history and exhumation process of the Horoman Peridotite Complex, Hokkaido, Japan, Tectonophysics, 379 (2004) 109–126.

[16] T. Mizukami, S. R. Wallis, J. Yamamoto, Natural examples of olivine lattice preferred orientation patterns with a flow-normal a-axis maximum, Nature, 427 (2004) 432–436.

[17] T. Tamimoto, D. Anderson, Mapping convection in the mantle, Geophys. Res. Lett., 11 (1984) 287–290.

[18] Y. Hiramatsu, M. Ando, T. Tsukuda, T. Ooida, Three-dimensional image of the anisotropic bodies beneath central Honshu, Japan, Geophys. J. Int., 135 (1998) 801–816.

[19] J. Polet, P. G. Silver, S. Beck, T. Wallace, G. Zandt, S. Ruppert, R. Kind, A. Rudloff, Shear wave anisotropy beneath the Andes from the BANJO, SEDA, and PISCO experiments, J. Geophys. Res., 105 (2000) 6287–6304.

[20] G. P. Smith, D. A. Wiens, K. M. Fischer, L. M. Dorman, S. C. Webb, J. A. Hildebrand, A complex pattern of mantle flow in the Lau Back arc, Science, 292 (2001) 713–716.

[21] V. Peyton, V. Levin, J. Park, M. Brandon, M. Lees, E. Gordeev, A. Ozerov, Mantle flow at slab edge: seismic anisotropy in the Kamchatka region, Geophys. Res. Lett., 28 (2001) 379–382.

[22] V. Levin, J. Park, J. Lees, M. T. Brandon, V. Peyton, E. Gordeev, A. Ozerov, Crust and upper mantle of Kamchatka from teleseismic receiver functions, Tectonophysics, 358 (2002) 233–265.

[23] V. Levin, D. Drozin, E. Gordeev, Detailed mapping of seismic anisotropy with local shear waves in southeastern Kamchatka, Geophys. J. Int., 158 (2004) 1009–1023.

[24] C. E. Hall, K. M. Fischer, E. M. Parmentier, D. K. Blackman, The influence of plate motions on three-dimensional back arc mantle flow and shear wave splitting, J. Geophys. Res., 105 (2000) 28009–28033.

[25] S. Karato, Mapping water content in the upper mantle, in: J. Eiler (ed.), Inside the subduction factory, AGU, Washington, D.C., 2003, Geophysical Monograph 138, pp. 135-149.

[26] B. K. Holtzman, D. L. Kohlstedt, M. E. Zimmerman, F. Heidelback, T. Hiraga, J. Hustoft, Melt segregation and strain partitioning: implications for seismic anisotropy and mantle flow, Science, 301 (2003) 1227–1230.

[27] S. Karato, On fabric transitions, Tectonophysics, (2005), In preparation.

[28] J. R. Mockel, Structural petrology of the garnet-peridotite of Alpe Arami (Ticino, Switzerland), Leidse Geologische, 42 (1969) 61–130.

[29] I. Katayama, S. Karato, Effects of temperature and stress on the deformation fabrics of olivine under hydrous conditions: An experimental study, Tectonophysics, (2005), In preparation.

[30] J. H. Davies, D. J. Stevenson, Physical model of source region of subduction zone volcanics, J. Geophys. Res., 97 (1992) 2037–2070.

[31] Y. Furukawa, S. Uyeda, Thermal structure under the tohoko arc with consideration of crustal heat generation, Tectonophysics., 164 (1989) 175–187.

[32] S. M. Peacock, K. Wang, Seismic consequences of warm versus cool subduction metamorphism: examples from southwest and northeast Japan, Science, 286 (1999) 937–939.

[33] J. A. Conder, D. Wiens, J. Morris, On the decompression melting structure at volcanic arcs and back-arc spreading centers, Geophys. Res. Lett., 29 (2002), doi: 10.1029/2002GL015390.

[34] C. A. Currie, J. F. Cassidy, R. D. Hyndman, M. G. Bostock, Shear wave anisotropy beneath the Cascadia subduction zone and western North American craton, Geophys. J. Int., 157 (2004) 341–353.

[35] P. E. van Keken, B. Kiefer, S. M. Peacock, High-resolution models of subduction zones: Implications for mineral dehydration reactions and the transport of water into the deep mantle, Geochem. Geophys Geosys., 3 (2002), doi:10.1029/2001DC000256.

[36] S. M. Peacock, R. D. Hyndman, Hydrous minerals in the mantle wedge and the maximum depth of subduction thrust earthquakes, Geophys. Res. Lett., 26 (1999) 2517–2520.

[37] A. G. Bostock, R. D. Hyndman, S. Rondenay, S. M. Peacock, An inverted continental Moho and serpentinization of the fore arc mantle, Nature, 417 (2002) 536–538.

[38] J. Park, H. Yuan, V. Levin, A serpentinite skidmark of trench-parallel terrane migration?, J. Geophys. Res., 109 (2004), doi:10.1029/2003JB002718.

[39] H. A. van der Vorst, Bi-CGSTAB: A fast and smoothly converging variant of Bi-CG for the solution of nonsymmetric linear systems, SIAM J. Sci. Comput., 12 (1992) 631–644.

[40] C. Cuvelier, A. Segal, A. A. van Steenhoven, Finite element methods and Navier-Stokes equations, Reidel Publishing, Dordrecht, Holland, 1986, pp. 483.

[41] G. Ranalli, Rheology of the Earth: Deformation and flow processes in geophysics and geodynamics, Allen and Unwin, Boston, 1987, pp. 366.

[42] H. Čížková, J. van Hunen, van den Berg, A. P., N. J. Vlaar, The influence of rheological weakening and yield stress on the interaction of slabs with the 670 km discontinuity, Earth Planet. Sci. Lett., 199 (2002) 447–457.

[43] S. Karato, H. Jung, Effects of pressure on high-temperature dislocation creep in olivine, Philosophical Magazine, 83 (2003) 401–414.

[44] S. Karato, P. Wu, Rheology of the upper mantle: a synthesis, Science, 260 (1993) 771–778.

[45] S. Franck, C. Bounama, Effects of water dependent creep rate on volatile exchange between mantle and surface reservoirs, Phys. Earth Planet. Inter., 92 (2000) 57–65.

[46] P. B. Kelemen, J. L. Rilling, E. M. Parmentier, L. Mehl, B. R. Hacker, Thermal structure due to solid-state flow in the mantle wedge beneath arcs, in: J. Eiler (ed.), Inside the subduction factory, AGU, Washington, D.C., 2003, Geophysical Monograph 138, pp. 293-311.

[47] G. Hirth, D. Kohlstedt, Rheology of the upper mantle and the mantle wedge: A view from the experimentalists, in: J. Eiler (ed.), Inside the subduction factory, AGU, Washington, D.C., 2003, Geophysical Monograph 103, pp. 83-105.

[48] Y. Furukawa, Depth of the decoupling plate interface and thermal structure under arcs, J. Geophys. Res., 98 (1993) 20005–20013.

[49] T. Takanami, I. S. Sacks, A. Hasegawa, Attenuation structure beneath the volcanic front in northeastern Japan from broad-band seismograms, Phys. Earth Planet. Inter., 121 (2000) 339–357.

[50] H. Zhang, C. H. Thurber, D. Shelly, I. Satoshi, G. C. Beroza, A. Hasegawa, High-resolution subducting-slab structure beneath northern Honshu, Japan revealed by double-difference tomography, Geology, 32 (2004) 361–364.

[51] J. C. Stachnik, G. A. Abers, D.Christensen, Seismic attenuation and mantle wedge temperatures in the Alaska subduction zone, J. Geophys. Res., 109 (2004), doi:10.1029/2004JB003018.

[52] E. Bonafede, M.and Boschi, M. Dragoni, Mechanical models of slow source processes, in: H. Kanamori, E. Boschi (eds.), Earthquakes; Observation, Theory and Interpretation, Scuola internazionale di fisica, 1983 .

[53] H. Kanamori, C. J. J., Focal process of the great Chilean earthquake May 22, 1960, Phys. Earth Planet. Int., 9 (1974) 128–136.

[54] T. Okada, T. Matsuzawa, A. Hasegawa, Shear-wave polarization anisotropy beneath the north-eastern part of Honshu, Japan, Geophys. J. Int., 123 (1995) 781–797.

[55] Abers, G., personal communication, 2004.

Figure1: Fabric maps of olivine for high-temperature (1470 K), high-stress experiments (left) (Jung and Karato, 2001). Spherical projections of a, b, and c axes are shown on the right. Shear direction is denoted with black arrows. The B-type fabric is observed at high-stress, relatively water-rich conditions and has an a-axis (fast axis) orientation that is sub-normal to the shear direction.

Figure2: Fabric map in temperature-stress space. Dotted and colored lines denote constant strain rate for power-law creep and Peierls creep. The thick black dashed line shows an extrapolation from experimental conditions to conditions of the mantle wedge. B-type fabric dominates to the left of this line while C-type fabric dominates temperature-stress space to the right. The transition temperature at mantle wedge stress (0.1-20 MPa) is predicted to be around 750-950 °C.

Figure 3: Diagram showing the kinematic-dynamic setup and implemented features (a). Partial viscous coupling is simulated by modifying boundary conditions along the top of the slab (b).

Figure 4: Model domain and discretization.

Figure 5: Steady-state calculations for temperature (a), strain rate (b), viscosity (c), and stress (d) for case 1.

Figure 6: Steady-state calculations for temperature (a), strain rate (b), viscosity (c), and stress (d) for case 2.

Figure 7: Steady-state calculations for temperature (a), strain rate (b), viscosity (c), and stress (d) for case 3.

Figure 8: Thermal models of Honshu, Japan for full viscous coupling at the base of a 40 km conducting lid (a) and 70 km partial viscous coupling (b). Dashed lines show the location of the top of the slab and base of the conducting lid. The volcanic front in denoted with a black triangle. Heat flow calculations (c) show a better match to observations, which are denoted with dashed boxes (data from Furukawa and Uyeda, 1989).

Figure 9: B-type fabric models for mantle wedge anisotropy. The transition from B-type conditions to conditions more suitable for C-type and other fabrics is denoted with the dashed line parallel to the trench. This figure shows end-member models for pure trench-normal flow (a) and slab-induced flow with a com-

ponent of trench-parallel flow (b). Partial coupling is denoted with a dashed line along the slab.

Table 1: Rheological Parameters	
$A_{disloc,dry}$	1.259×10^{-12} s^{-1} Pa^{-3}
$E_{disloc,dry}$	5.1×10^{5} J / mol
$V_{disloc,dry}$	14×10^{-6} m^{3} / mol
$A_{disloc,wet}$	3.631×10^{-18} s^{-1} Pa^{-3}
$E_{disloc,wet}$	4.1×10^{5} J / mol
$V_{disloc,wet}$	11×10^{-6} m^{3} / mol
$A_{diff,dry}$	1.088×10^{5} s^{-1} Pa^{-1}
$E_{diff,dry}$	3.0×10^{5} J / mol
$V_{diff,dry}$	6×10^{-6} m^{3} / mol
$A_{diff,sat}$	6.625×10^{4} s^{-1} Pa^{-1}
$E_{diff,sat}$	2.4×10^{5} J / mol
$V_{diff,sat}$	5×10^{-6} m^{3} / mol
n	3.0
r	1.2
q	1.2
b	0.5 x 10^{-9} m
d	1 mm
m	2.5
τ_y	100 MPa
$\dot{\epsilon}_y$	10^{-14} s^{-1}
n_y	5
C_{OH}^{max}	5000 ppm H/Si

Table 2: Model Parameters					
parameter	case 1	case 2	case 3	case 4	case 5
velocity (cm / yr)	8	8	8	9.1	9.1
age of lithosphere (Ma)	50	50	50	130	130
crustal conductivity (W/m/K)	3.1	3.1	3.1	2.5	2.5
mantle conductivity (W/m/K)	3.1	3.1	3.1	3.1	3.1
water content (ppm H/Si)	0	1000	1000	1000	1000
slab geometry	45°	45°	45°	polynomial	polynomial

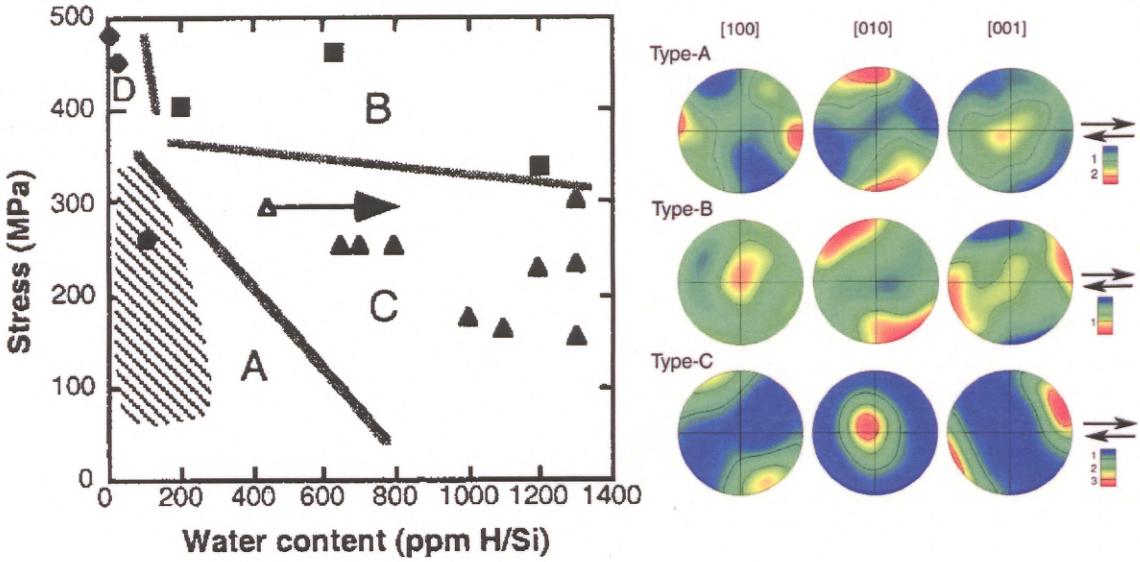
500
400
300
200
100
0
Stress (MPa)
D
B
C
A
0
200
400
600
800
1000
1200
1400
Water content (ppm H/Si)
[100]
[010]
[001]
Type-A
Type-B
Type-C
1
2
1
1
2
3

Figure 1:

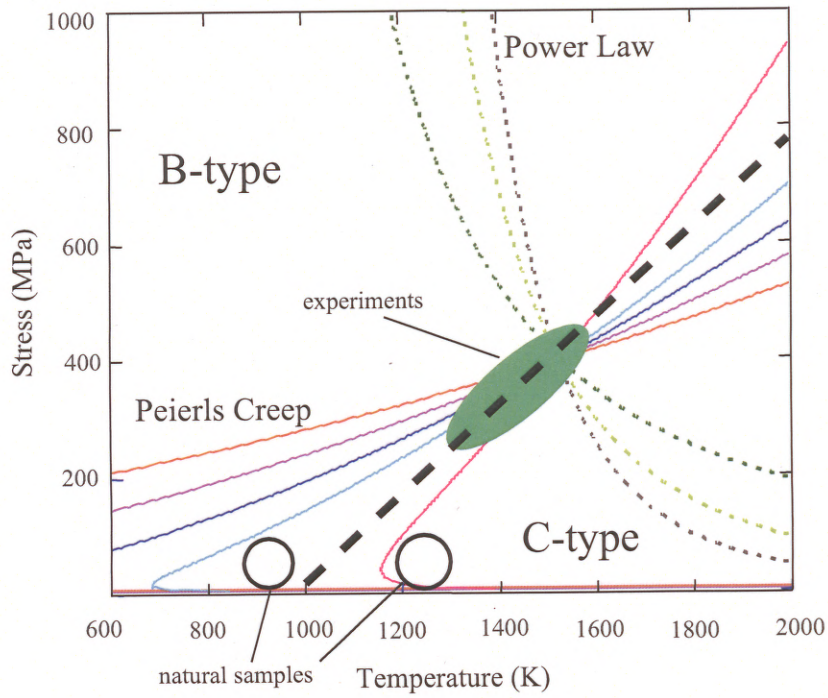
1000
800
600
400
200
Stress (MPa)
B-type
Power Law
experiments
Peierls Creep
C-type
600
800
1000
1200
1400
1600
1800
2000
natural samples
Temperature (K)

Figure 2:

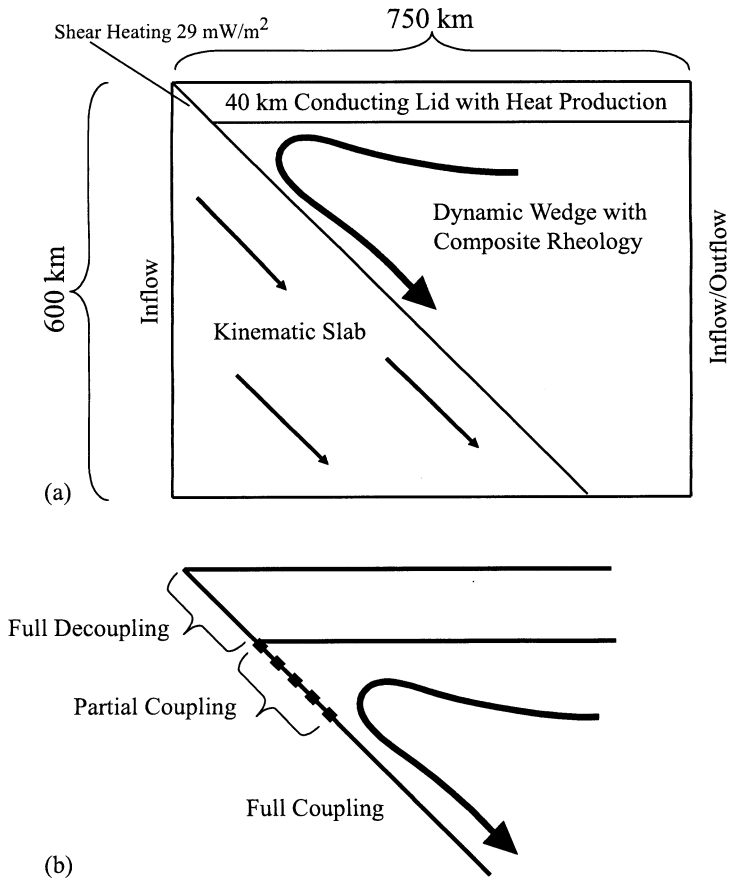
Shear Heating 29 mW/m2
750 km
40 km Conducting Lid with Heat Production
Dynamic Wedge with
Composite Rheology
600 km
Inflow
Kinematic Slab
Inflow/Outflow
(a)
Full Decoupling
Partial Coupling
Full Coupling
(b)

Figure 3:

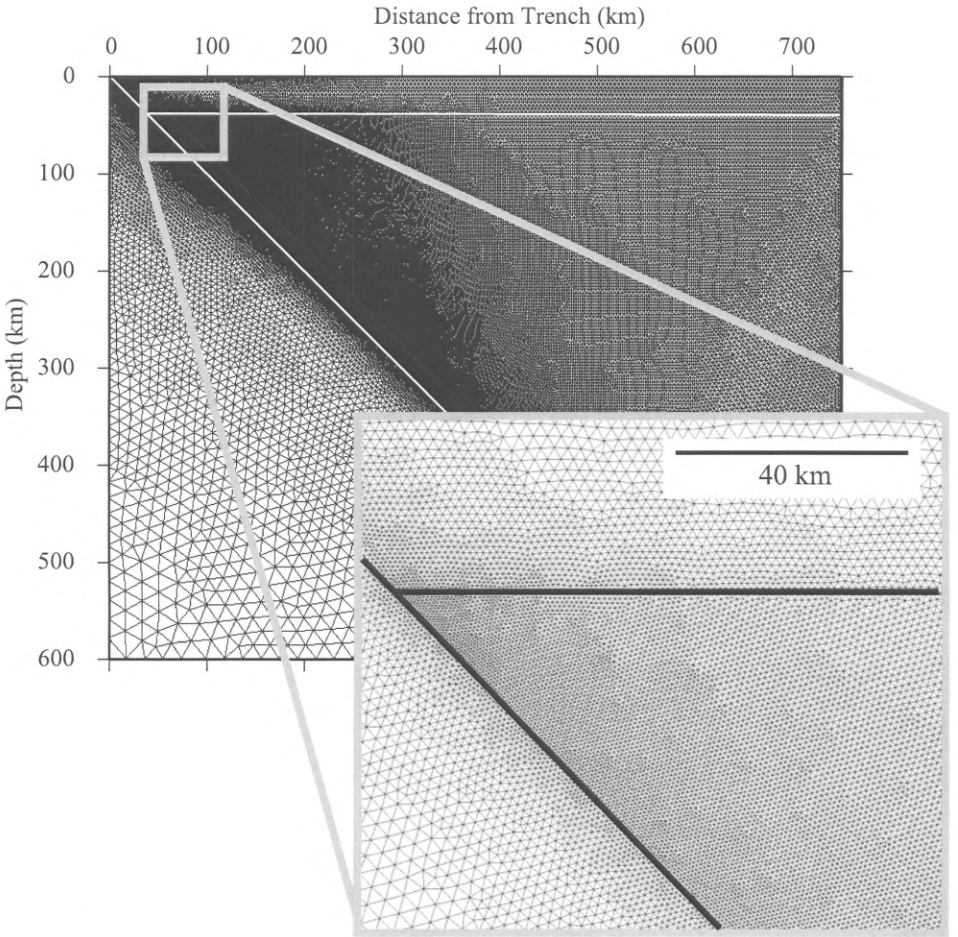
Distance from Trench (km)
0
100
200
300
400
500
600
700
Depth (km)
0
100
200
300
400
500
600
40 km

Figure 4:

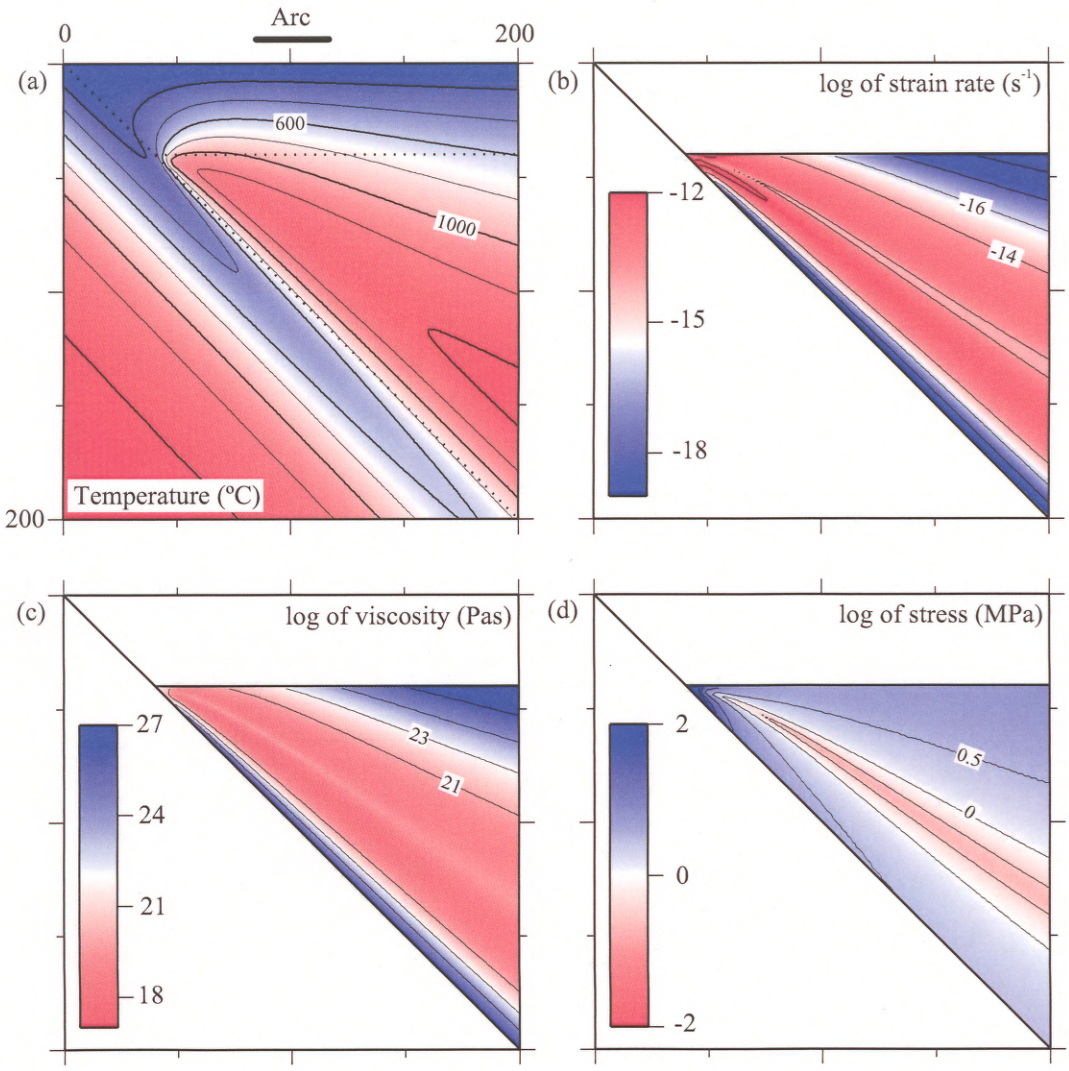
Arc
0
200
(a)
600
1000
Temperature (°C)
200
(b)
log of strain rate (s-1)
-12
-15
-18
-16
-14
(c)
log of viscosity (Pas)
27
24
21
18
23
21
(d)
log of stress (MPa)
2
0
-2
0.5
0

Figure 5:

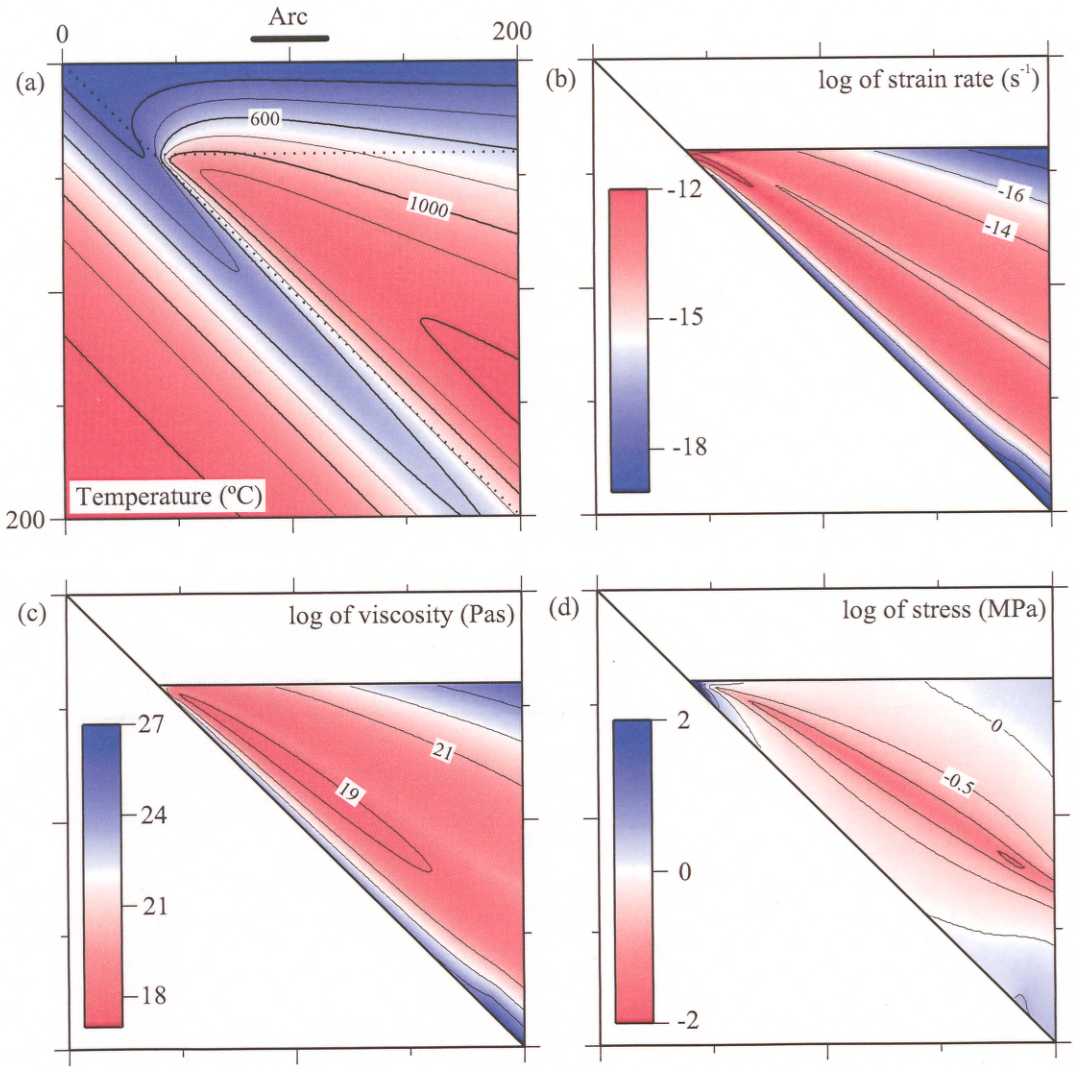
Arc
0
200
(a)
600
1000
Temperature (°C)
200
(b)
log of strain rate (s-1)
-12
-15
-18
-16
-14
(c)
log of viscosity (Pas)
27
24
21
18
21
19
(d)
log of stress (MPa)
2
0
-2
0
-0.5

Figure 6:

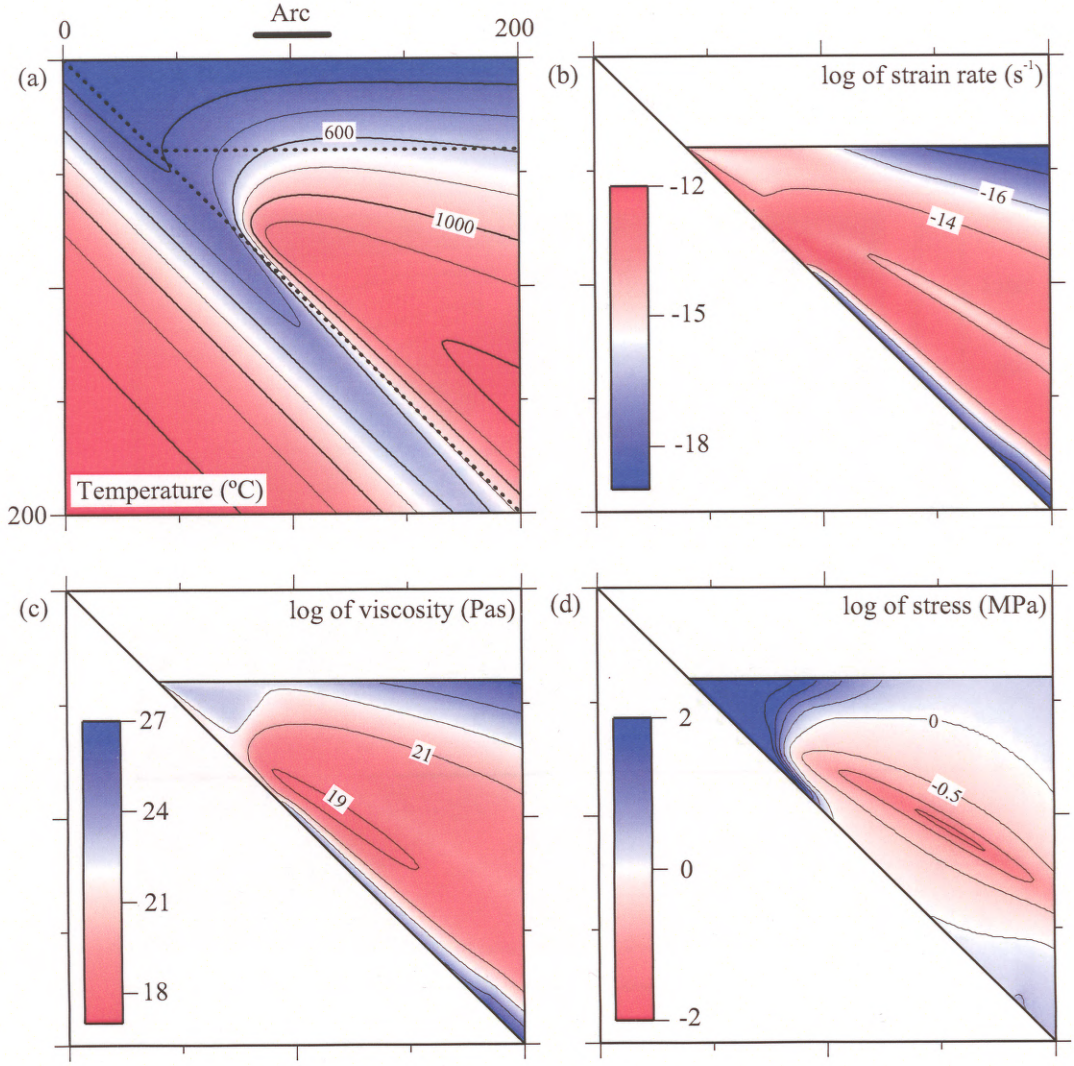
Arc
0
200
(a)
600
1000
Temperature (°C)
200
(b)
log of strain rate (s-1)
-12
-15
-18
-16
-14
(c)
log of viscosity (Pas)
27
24
21
18
21
19
(d)
log of stress (MPa)
2
0
-2
0
-0.5

Figure 7:

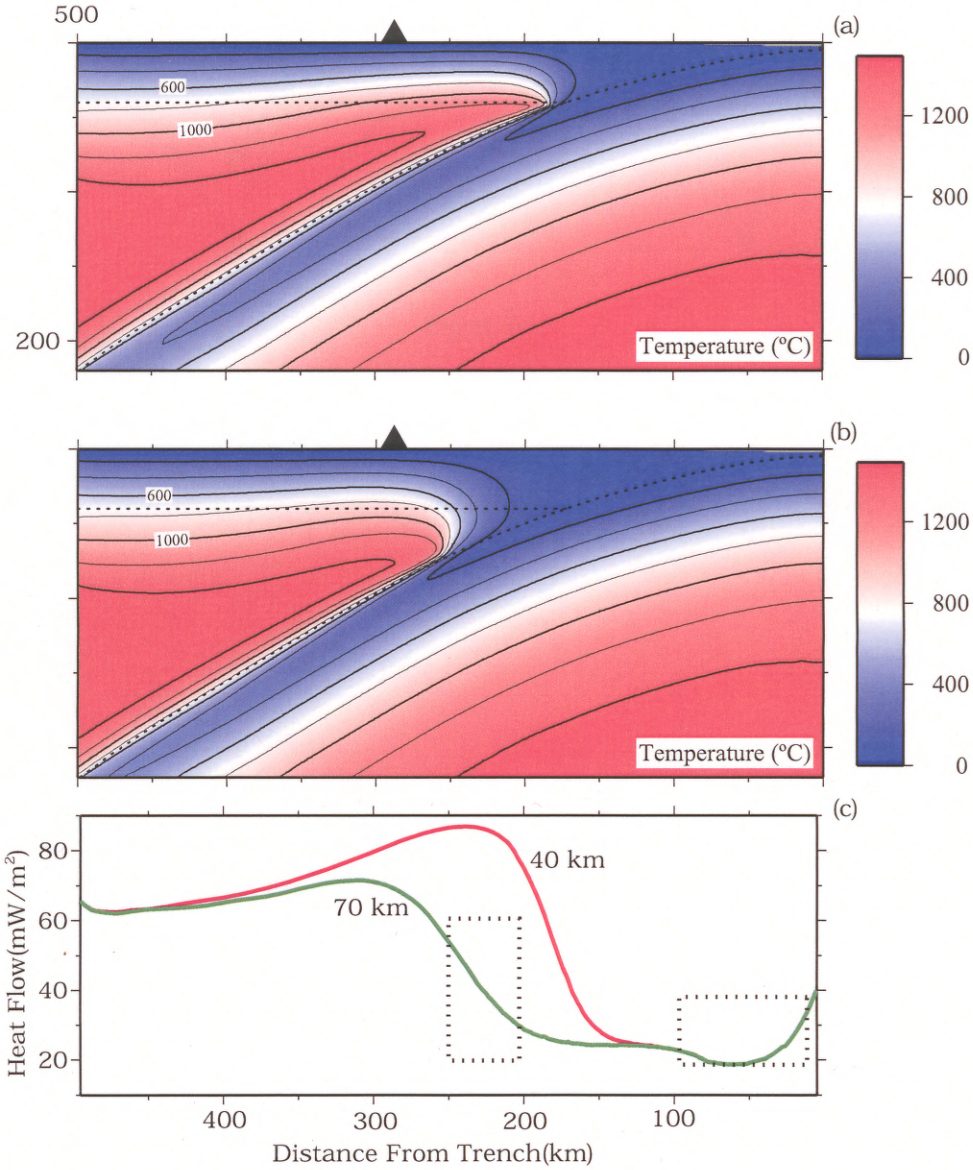
500
200
(a)
600
1000
Temperature (°C)
1200
800
400
0
(b)
600
1000
Temperature (°C)
1200
800
400
0
(c)
Heat Flow(mW/m²)
80
60
40
20
40 km
70 km
400
300
200
100
Distance From Trench(km)

Figure 8:

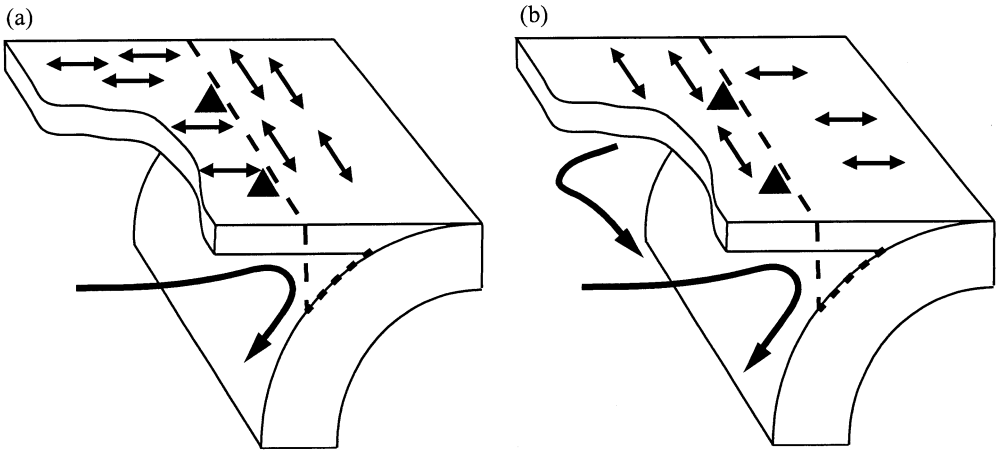

Figure 9: